Journal of Solid State Chemistry 182 (2009) 1838–1845

Contents lists available at ScienceDirect

Journal of Solid State Chemistry

journal homepage: www.elsevier.com/locate/jssc

Doped titanium dioxide nanocrystalline powders with high photocatalytic activity

A.L. Castro [a], M.R. Nunes [b], M.D. Carvalho [b,*], L.P. Ferreira [c,d], J.-C. Jumas [e], F.M. Costa [b], M.H. Florêncio [a]

[a] *CQB/Dep. Química e Bioquímica, Faculdade de Ciências, Universidade de Lisboa, Campo Grande, Ed. C8, 1749-016 Lisboa, Portugal*
[b] *CCMM/Dep. Química e Bioquímica, Faculdade de Ciências, Universidade de Lisboa, Campo Grande, Ed. C8, 1749-016 Lisboa, Portugal*
[c] *CFMC-Universidade de Lisboa, Faculdade de Ciências, Campo Grande, Ed. C8, 1749-016 Lisboa, Portugal*
[d] *Dep. Física, Faculdade de Ciências e Tecnologia, Universidade de Coimbra, 3004-516 Coimbra, Portugal*
[e] *Institut Charles Gerhardt (UMR 5253) Université Montpellier 2, Place E. Bataillon, 34095 Montpellier Cedex 5, France*

ARTICLE INFO

Article history:
Received 24 January 2009
Received in revised form
15 April 2009
Accepted 19 April 2009
Available online 3 May 2009

Keywords:
Doped titanium dioxide
Anatase phase
Nanocrystalline
Hydrothermal synthesis
Photocatalytic activity

ABSTRACT

Doped titanium dioxide nanopowders (M:TiO_2; $M=$ Fe, Co, Nb, Sb) with anatase structure were successfully synthesized through an hydrothermal route preceded by a precipitation doping step. Structural and morphological characterizations were performed by powder XRD and TEM. Thermodynamic stability studies allowed to conclude that the anatase structure is highly stable for all doped TiO_2 prepared compounds. The photocatalytic efficiency of the synthesized nanopowders was tested and the results showed an appreciable enhancement in the photoactivity of the Sb:TiO_2 and Nb:TiO_2, whereas no photocatalytic activity was detected for the Fe:TiO_2 and Co:TiO_2 nanopowders. These results were correlated to the doping ions oxidation states, determined by Mössbauer spectroscopy and magnetization data.

1. Introduction

Semiconductor photocatalysis has been the subject of many research studies due to its wide application on the elimination of hazardous pollutants from air, soil and water [1–3]. Among various oxide semiconductor photocatalysts, titanium dioxide (TiO_2) has been extensively investigated and proved to be the most suitable catalyst for heterogeneous photocatalytic oxidation due to its high photoactivity, thermal and chemical stability, low cost and non-toxicity [4–6].

The activation of TiO_2 for photocatalytic reactions is achieved upon irradiation with an energy value equal or greater than the one of its band gap (E_g). Thus, electron charge transfer from valence band to conduction band occurs, resulting in the creation of electron–hole pairs (e^-/h^+). These excited charge carriers can migrate and then react with molecules adsorbed on the semiconductor surface [6–8], or can recombine either at the bulk or at the surface of the oxide, dissipating the input energy as heat, thereby contributing to the deactivation of the semiconductor. Thus, photocatalytic efficiency of TiO_2 depends on several factors, such as: the electron–hole pair production capacity, the separation efficiency of the photogenerated charge pair and the charge transfer efficiency of the charge carriers to compounds adsorbed on the TiO_2 surface [9]. Additionally, the high bandgap energy ($E_g = 3.2\,eV$; $\lambda = 387\,nm$) of TiO_2 clearly limits its efficient solar energy applications once only *ca.* 3% of the solar light could be absorbed. In order to overcome these limitations, many investigations on modified TiO_2 systems have been carried out [10–18] to extend the photoresponse of TiO_2 to the visible region. Its photoactivity could then be improved by reducing the recombination rate of the electron–hole pairs and by enhancing the interfacial charge transfer efficiency. Recent studies show that the doping of crystalline TiO_2 lattice with transition metal ions, by maintaining good control of the nanoscale particle size, is a promising methodology that permits the TiO_2 electronic structure change and consequently a reduction of the above mentioned limitations [19–23]. The substitutional doping of TiO_2 with transition metal ions induces electronic coupling effects with the host atom and leads to the creation of electron states within the oxide band gap. Jasra et al. [23] explained that localized states of the dopant can either shift towards the TiO_2 conduction band or the valence band edge. If the energy level of dopant ions shifts to the conduction band edge, the efficiency of trapping becomes higher, thus reducing the electron–hole recombination rate.

It has been also demonstrated that the preparative methodology of the materials plays a key role for optimization of its physicochemical and catalytic characteristics [17]. Many controversial results are reported in the literature regarding the fact that

---

[*] Corresponding author. Fax: +351 21 750 00 88.
E-mail address: mdcarvalho@fc.ul.pt (M.D. Carvalho).

0022-4596/$ - see front matter © 2009 Elsevier Inc. All rights reserved.
doi:10.1016/j.jssc.2009.04.020

the catalysts properties are strongly dependant on the method of doping [24].

Hydrothermal method has already been used to synthesize nanosized TiO_2, since products prepared by this method are well-crystallized and have small crystallite size, which benefit the thermal stability and photocatalytic activity [25]. The doping of TiO_2 using the presently reported synthesis, however, has just a few reports [26–28].

In the present work highly pure and stable anatase doped titanium dioxide nanopowders (M:TiO_2; $M=$ Fe, Sb, Nb, Co) have been prepared by means of an hydrothermal methodology recently reported [25,29]. The developed procedure is simple, low cost, and is a low temperature synthesis technique which avoids the use of hazardous chemical compounds. The synthesized powders were structurally, morphologically and optically characterized and its photocatalytic properties studied.

2. Experimental

2.1. Synthesis

The M:TiO_2 ($M=$ Fe, Co, Nb, Sb) nanopowders were prepared by means of a recently published method [25,29]. All the reagents used in the synthesis experiments were purchased from commercial sources and used without further purification. The dopant starting materials were metallic cobalt (Co, Johnson Matthey) and iron (Fe, Johnson Matthey), antimony ethoxide ($Sb(OC_2H_5)_3$, Aldrich) and niobium pentachloride ($NbCl_5$, Aldrich). A titanium trichloride solution ($TiCl_3$, 10 wt% in 20–30 wt% HCl, Aldrich) diluted in a ratio of 1:2 in standard (2 M) hydrochloride acid (37% HCl, Panreac) was used as the titanium source. The molar amount of transition metal ion dopant was calculated in order to substitute 5% of titanium ions in TiO_2 and was solubilized in nitric acid (HNO_3, Merck) or hydrochloric acid (HCl, Panreac). This solution was added to the titanium trichloride solution (doping step). Then, the amount of an ammonium solution (4 M, Merck) necessary to ensure total precipitation was added dropwise under vigorous stirring. The resulting suspension was maintained at room temperature overnight, filtered and vigorously washed with deionized water. The aqueous suspensions of the doped TiO_2 samples were heated at 200 °C for 6 h in an autoclave. The final powders were obtained by dehydration in an oven.

The undoped TiO_2 was prepared using the same method for comparative purposes.

2.2. Characterization

The crystal structure and phase purity of the powders were checked by X-ray powder diffraction (XRD) with a Phillips PW 1730 diffractometer using a Cu$K\alpha$ radiation, previously calibrated using a Si standard. The accelerating voltage of 40 kV and emission current of 30 mA were used. Data were collected in the range 20–80° (2θ) in a step-scan mode, with a step size of 0.02°. In order to obtain more reliable results, the cell parameters were determined using the profile mode of FullProf software [30]. A sixth order polynomial function was used to model the background level and the peak shapes were fitted to a pseudo-Voigt function.

The morphology and mean particle size of the samples were analysed by transmission electron microscopy (TEM). TEM observations were carried out on a Hitachi H-8100 system operating at 200 V. Samples were prepared by evaporation of very diluted aqueous suspensions onto carbon-coated copper grids (400 mesh) covered by a thin layer of Formvar with carbon.

The average transition metal content of samples was determined with an energy dispersive X-ray (EDS) detector (Thermo-NORAN D-3756) attached to the TEM system.

The ^{121}Sb Mössbauer measurements were carried out in standard transmission geometry, using a $Ba^{121m}SnO_3$ source. During the measurements, both the source and the absorber were simultaneously cooled (4 K) to increase the fraction of recoil-free absorption and emission processes. The velocity scale was calibrated with the standard spectrum of an iron absorber using a ^{57}Co(Rh) source. The Mössbauer parameters, isomer shift (δ), quadrupole splitting (Δ) and absorber linewidth (Γ), were obtained from the experimental data by using the GM5SIT software [31]. The zero isomer shift was defined from the spectrum of InSb at 4 K ($\delta=-8.27$ (4) mm/s relative to the $Ba^{121m}SnO_3$ source). The ^{57}Fe Mössbauer spectrum was collected at room temperature in transmission mode using a conventional constant-acceleration spectrometer and a 25 mCi ^{57}Co source in a Rh matrix. The velocity scale was calibrated using an α-Fe foil. The spectrum was fitted to a distribution of quadrupole splittings according to the histogram method.

Magnetization measurements were carried out in powder samples of Fe and Co doped TiO_2 and undoped TiO_2 for comparison. Magnetization data were collected using a SQUID magnetometer (Quantum Design MPMS) over the temperature range from 2 to 300 K, at applied magnetic fields up to 5.5 T. The data were analysed using the spin-Hamiltonian model, to obtain information on the amount of the metallic ions and their oxidation states. Further details on data collection and fitting procedure can be found in the literature [32].

The optical characterization of the powders was carried out by UV–Vis diffuse reflectance spectroscopy (DRS) on a Jasco V560 spectrophotometer equipped with an integrating sphere attachment. Spectra were recorded in the 300–600 nm wavelength range, in the diffuse reflectance mode. The bandgap energies of the doped TiO_2 were estimated assuming direct bandgap transition. Thus, bandgap energies were estimated by the straight-line intercept fitted to a graph of $[F(R)*h\nu]^2$ versus $h\nu$, where $F(R)$ is the Kubelka–Munk function [33] and $h\nu$ is the energy of the incident photon.

2.3. Photocatalytic experiments

Diquat dibromide monohydrate (Sigma-Aldrich) was chosed as model compound, due to our good knowledge of its degradation using commercial TiO_2 (P25 from Degussa) as calatyst [34]. The photocatalytic behaviour of selected hydrothermally synthesized M:TiO_2 nanosamples was evaluated on the degradation of *diquat* aqueous solutions (10^{-4} M) under UV conditions. The activity of these catalysts was compared with that of commercial TiO_2 and of the prepared undoped TiO_2. The catalysts were used as a 0.2 g L^{-1} suspension. The samples were contained in quartz crystallization dishes, covered with transparency film to allow easy collection of aliquots during irradiation. The solutions were homogenized with magnetic stirrers, for approximately 60 min in the dark, to achieve an adequate equilibrium of adsorption/desorption of the herbicide on the photocatalyst, prior to irradiation. The artificial radiation source used was a high pressure mercury 125 W lamp, from Philips, emitting in the range $300\,nm<\lambda<400\,nm$, with an average flux of about 126 klx. The total photonic flux was measured by means of an UV and light smart meter from Oriel with a Goldilux light probe. The UV experiments were carried out on an UV–visible Jasco Spectrophotometer Model V560. The concentration of *diquat* was calculated from the absorption band at 309 nm.

3. Results and discussion

3.1. X-ray diffraction (XRD)

Powder X-ray diffraction (XRD) was used to verify the purity of the hydrothermally synthesized doped TiO_2 (M:TiO_2) and to determine the cell parameters values. The XRD patterns of the examined samples are depicted in Fig. 1, where the XRD pattern of the undoped TiO_2 sample was included for comparative purposes. All the patterns indicate the formation of single anatase phase (JCPDS Card no. 21-1272) as no other additional diffraction peaks were detected within the X-ray detection limit.

The effect of the transition metal substitution in the TiO_2 lattice on the cell parameters (a and c), determined by refinement of the XRD patterns, is shown in Table 1. While lattice parameter a remains almost unchanged, a slightly increase of anatase lattice parameter c is observed for all doped samples, in comparison to the undoped TiO_2 data, resulting in a small lattice expansion. This behaviour is consistent with the presence of doping ions in the TiO_2 lattice.

According to thermodynamic data, rutile is the most stable phase over a wide range of temperatures. It was previously reported [35] that titania normally undergoes anatase-to-rutile phase transformation when the temperature is raised above 450 °C, at least. Nevertheless, it was earlier demonstrated [25] that the use of mild hydrothermal synthesis conditions, allows to obtain pure and stable nanosized TiO_2 anatase phase until 800 °C. In order to study the stability of the prepared M:TiO_2 samples, the powders were calcinated under different temperatures ranging from 500 to 1100 °C. The XRD patterns of this study, presented in Fig. 2, clearly show that all doped samples obtained by this method stabilize in the anatase phase up to a temperature value significantly higher than 450 °C. Nevertheless, different behaviours were observed depending on the doping metal. In the case of Nb:TiO_2 and Sb:TiO_2 phases, anatase structure remains pure and stable until 900 and 800 °C, respectively. Afterwards, the rutile conversion starts and, at 1100 °C, the anatase to rutile phase transition is completed for both samples. In the case of the Fe:TiO_2 and Co:TiO_2, simultaneously with the phase transition, which was completed at 1100 °C, new peaks were observed on the XRD patterns, detected at 700 °C in the case of Co:TiO_2 and at 1100 °C in the case of the Fe:TiO_2 sample. These peaks were attributed to the presence of Fe_2TiO_5 and $CoTiO_3$ crystalline phases (JCPDS-File no. 9-182 and 15-866, respectively). Besides, it should be noted that the anatase to rutile phase transition is observed at 800 °C for the cobalt containing compound and at 1000 °C for Fe:TiO_2, indicating a lower stability for the cobalt doped compound. This is probably due to the strain energy associated with the incorporation of Co ions in the TiO_2 lattice as previously stated [36].The presence of a poor crystallized cobalt phase cannot be disregarded, however, as this hypothesis would explain the segregation of $CoTiO_3$ observed at 700 °C, before the anatase to rutile phase transition begins. These results also allow to conclude that the metal ions effectively substitute the titanium ions in the TiO_2 lattice, although most probably in a slightly lower amount for the Fe:TiO_2 and Co:TiO_2 samples.

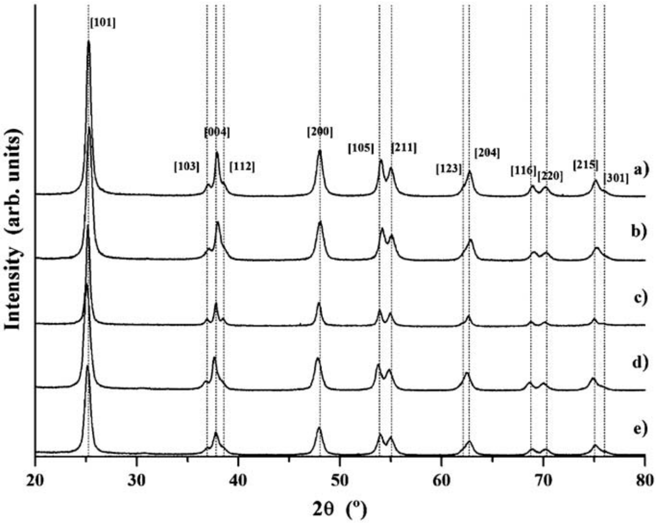

Fig. 1. Powder X-ray patterns for the titania samples hydrothermally synthesized for 6 h at 200 °C: (a) Sb:TiO_2, (b) Co:TiO_2, (c) Fe:TiO_2, (d) Nb:TiO_2 and (e) undoped TiO_2. The standard XRD pattern for anatase is plotted from JCPDS Card no. 21-1272 (dash lines).

Table 1
Cell parameters of hydrothermally synthesized M:TiO_2 powders.

Sample	a (Å)	c (Å)	Cell volume (Å^3)
TiO_2	3.7821(2)	9.4776(2)	135.57(1)
Fe:TiO_2	3.7910(2)	9.5034(5)	136.58(5)
Sb:TiO_2	3.7896(2)	9.4875(4)	136.25(1)
Nb:TiO_2	3.7871(3)	9.4952(8)	136.18(2)
Co:TiO_2	3.7898(2)	9.4770(4)	136.11(1)

3.2. Transmission electron microscopy (TEM)

TEM analysis revealed the morphology of the samples and allowed straightforward deduction of mean particle size by direct sample observation. Fig. 3 shows the TEM images obtained for synthesized M:TiO_2 materials. It is possible to observe that all the samples present poor homogeneity and narrow particle size distribution. The mean particle size values, summarized in Table 2, were obtained as the average of the measured size of a significant number of particles that could be clearly identified on every display. Images of Fe:TiO_2 and Sb:TiO_2 nanopowders, Fig. 3a and b, respectively, show a morphology similar to that previously observed for the undoped phase TiO_2 [25] whereas Nb:TiO_2 and Co:TiO_2 nanopowders, Fig. 3c and d, respectively, present particles with an elongated morphology.

Energy dispersive X-ray (EDS) investigations (via TEM mode) were carried out on the synthesized samples in order to determine the relative amount of metal content. The resulting spectra (not shown) clearly indicated the presence of the doped metals, with M/Ti atomic ratios values varying from 4% (Fe and Co) to 5% (Sb and Nb). It should be noted that the metal ion dopant distribution in nanopowders are randomized. Thus, the metal content obtained by EDS analysis represents a mean value close to the nominal one.

3.3. Mössbauer spectroscopy

The presence of both iron and antimony ions in the doped samples is supported by the Mössbauer spectroscopy measurements which spectra are presented in Fig. 4.

In the case of the Fe:TiO_2 compound, the obtained spectrum, Fig. 4(a), undoubtedly shows that only Fe^{III} is present in the sample, the isomer shift (δ) value being characteristic of Fe^{III} in octahedral coordination (Table 3). The distribution obtained in the quadrupole splitting values is consistent with slightly different Fe environments, most probably due to different nanocrystallite sizes.

The ^{121}Sb Mössbauer spectrum is shown in Fig. 4(b) and the corresponding refined hyperfine parameters are included in

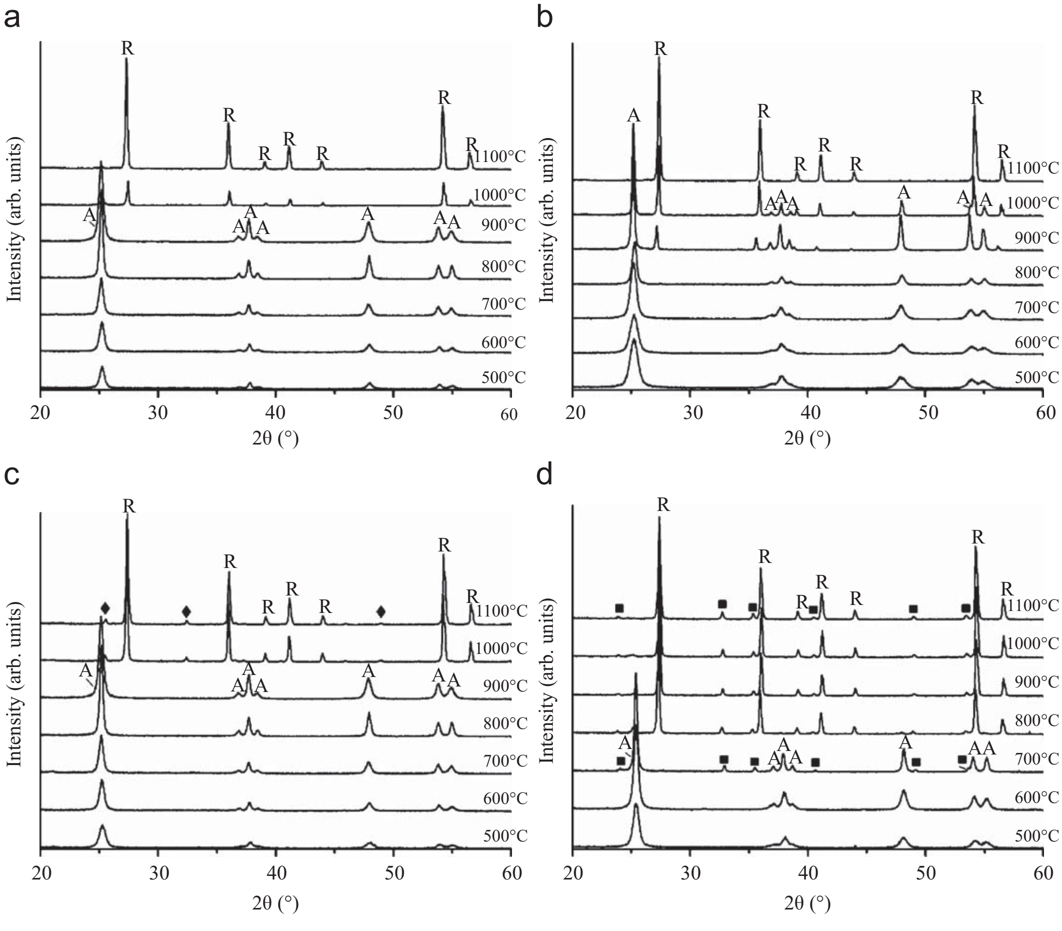

Fig. 2. XRD patterns of M:TiO_2 calcinated at 500–1100 °C: (a) Nb:TiO_2 (b) Sb:TiO_2, (c) Fe:TiO_2, (d) Co:TiO_2. (A—anatase phase; R—rutile phase; ■—$CoTiO_3$ phase; and ♦—Fe_2TiO_5 phase).

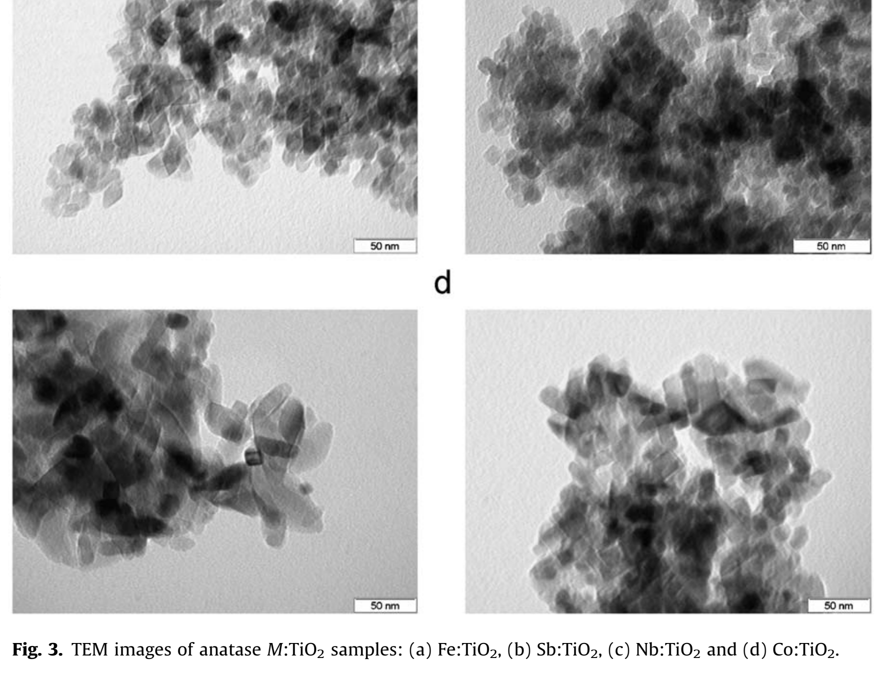

Fig. 3. TEM images of anatase M:TiO_2 samples: (a) Fe:TiO_2, (b) Sb:TiO_2, (c) Nb:TiO_2 and (d) Co:TiO_2.

Table 2
Mean particle size of the *M*:TiO_2 powders.

Sample	Mean particle size (nm)
TiO_2 [26]	≈14
Fe:TiO_2	≈11
Sb:TiO_2	≈9
Nb:TiO_2	≈13
Co:TiO_2	≈13

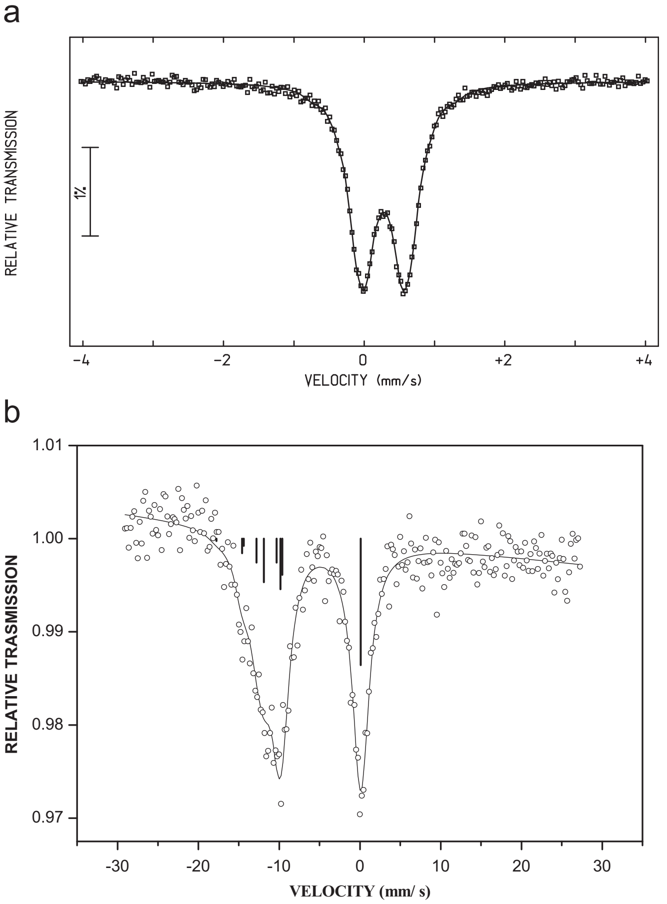

Fig. 4. ^{57}Fe and ^{121}Sb Mössbauer spectra of Fe:TiO_2 (a) and Sb:TiO2 (b). The velocity scale has not been corrected for InSb reference (−8.27(4) mm/s relative to the source). The bar diagram on the ^{121}Sb spectrum shows the different contributions of each sub spectra.

Table 3. The spectrum clearly shows the presence of the two oxidation states for antimony (III and V) with hyperfine parameters, respectively, close to those related for Sb_2O_3 ($\delta = -3.30(7)$ mm/s, $\Delta = +18.2(5)$ mm/s) and for Sb_2O_5 ($\delta = +9.21(6)$ mm/s, $\Delta = -4.3$ mm/s) [37]. As it can be assumed that at 4 K the recoil-free fractions for Sb^{III} and Sb^{V} atoms in non-equivalent crystallographic sites are more or less equal, the Sb^{III}/Sb^{V} area ratio of the absorption peaks (1.60) corresponds to the area ratio obtained in this mixed valence sample. For Sb^{III} the large value of Δ is in agreement with a distorted environment and a high stereochemical activity of the Sb lone pair, as in the case of Sb_2O_3, whereas for Sb^{V}, $\Delta = 0$ indicates an undistorted octahedral environment.

3.4. Magnetic measurements

The magnetization curves show that besides the paramagnetic signal due to the presence of iron and cobalt ions, a diamagnetic temperature independent contribution was detected in all samples. This contribution corresponds to metallic ions with closed electronic shells and is the foremost magnetic component in the undoped TiO_2 sample. For each magnetization versus temperature curve, collected at a certain magnetic field, the diamagnetic fraction was determined from the value of the intercept I in the plot of the magnetic susceptibility χ versus inverse temperature ($\chi = C/T+I$), in the temperature region where the Curie law is valid, and subtracted from the total magnetic signal. After subtraction of the diamagnetic component, the analysis of the magnetization curves using the spin-Hamiltonian model indicates that in the Fe:TiO_2 doped sample, Fig. 5(a), around 4% of iron ions were detected, in good agreement with EDS results. Moreover, the magnetization data is consistent with all iron ions in high spin oxidation state III ($S = \frac{5}{2}$), in accordance with Mössbauer results. In the Co-doped material, Fig. 5(b), the best

Table 3
^{57}Fe and ^{121}Sb Mössbauer parameters of Fe:TiO_2 and Sb:TiO_2.

Sample	δ (mm/s)	Δ (mm/s)	Γ (mm/s)	Contribution (%)	Attribution
Fe:TiO_2	0.379 (1)	0.669 (1)	0.30	100	Fe^{III} (octahedral)
Sb:TiO_2	−2.96 (7)	+16.6 (7)	1.06 (9)	61.5 (8)	Sb^{III} type Sb_2O_3
	+8.39 (4)	–	1.06 (9)	38.5 (8)	Sb^{V} type Sb_2O_5

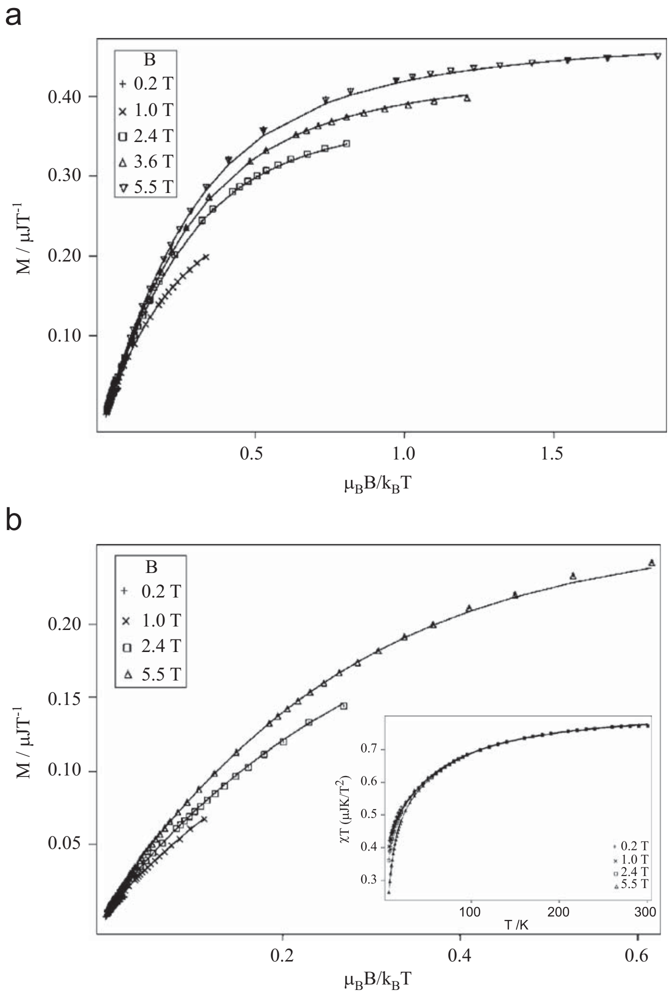

Fig. 5. Magnetization of Fe:TiO_2 (a) and of Co:TiO_2 (b) plotted against $\mu_B B/k_B T$, collected at different magnetic applied fields, between 2 (or 5, in the case of (b)) and 300 K, after subtraction of the diamagnetic fraction. The solid lines correspond to least square fitting with the spin-Hamiltonian model. The inset in (b) shows χT versus temperature.

fitting results were obtained when only cobalt ions in high spin oxidation state IV, $S = \frac{5}{2}$, were considered. However, the amount obtained from the fitting procedure corresponds only to 2% of the total Co content detected by EDS. This discrepancy is explained by the presence of cobalt ions in low spin oxidation state III, which corresponds to spin zero, contributing to the diamagnetic component referred above. In fact, high spin Co^{IV} (d^5) and low spin Co^{III} (d^6) are the most energetically favourable configurations. Although Co^{III} is generally accepted as the most probable oxidation state for cobalt ions, the presence of the unusual Co^{IV} ions is acceptable due to the hydrothermal method used in the synthesis procedure.

The possible presence of Co^{II} ions in low spin state $S = \frac{1}{2}$ due to impurities like $CoTiO_3$ can be ruled out, since it would give rise to no splitting of the magnetization curves. These results also show that the $CoTiO_3$ impurity is not present in the prepared Co:TiO_2 powder, and is only formed after the thermal treatment around 700 °C (Fig. 2).

3.5. UV–Vis diffuse reflectance spectra

It is well known that the photocatalytic activity of a semiconductor is related to its bandgap structure. The UV–Vis spectra of the synthesized doped nanopowders are shown in Fig. 6. For comparison, the spectrum of the undoped TiO_2 is also shown. All doped powders show enhanced absorption in the range 400–600 nm, with higher increase for samples containing iron, niobium and antimony. In Co:TiO_2 spectrum a convolution of absorbances is observed. This observation can be due to non-homogeneously distribution of cobalt ions in the TiO_2 lattice, in accordance with the stability tests results of this powder. For Fe:TiO_2 a broad band centred at ca. 480 nm is visible and attributed to d-d transitions, as explained in the literature [26].

To establish the type of bandgap transition for the synthesized nanopowders, the diffuse reflectance data were fitted to equations for both indirect and direct bandgap transitions. The profiles show perfect fit for direct bandgap transition and the calculated E_g values for each powder are reported in Table 4. The hydrothermally doped titania powders show E_g values equal (Nb:TiO_2) or lower (Sb:TiO_2, Fe:TiO_2 and Co:TiO_2) than the one for the undoped titania powder, consistent with the red shift of absorption edge observed. These red shifts can be attributed to the charge transfer transitions between the metal ion d electrons and the conduction band or valence band of TiO_2 [19].

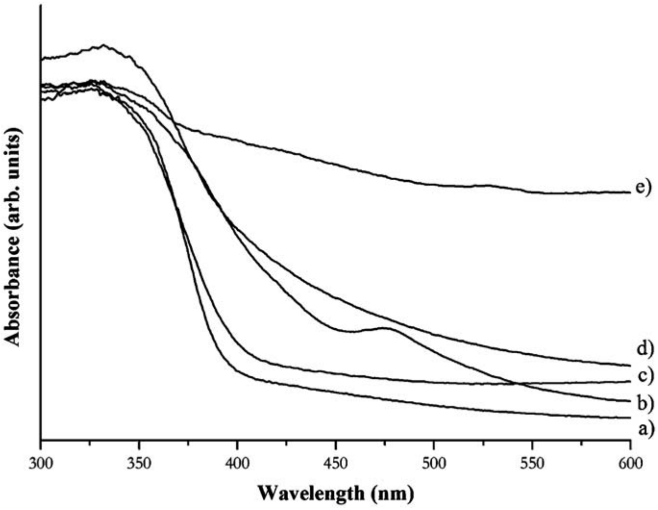

Fig. 6. Diffuse reflectance spectra of hydrothermally synthesized M:TiO_2 samples: (a) undoped TiO_2, (b) Fe:TiO_2, (c) Nb:TiO_2, (d) Sb:TiO_2 and (e) Co:TiO_2.

Based on the E_g and absorption edge values obtained, the photocatalysts were expected to be active under UV irradiation, and, in the case of Fe:TiO_2 and Co:TiO_2, also under visible light. Therefore, these two catalysts were also tested under visible irradiation.

3.6. Photocatalytic results

The photocatalytic activity of the synthesized doped and undoped titania nanopowders was undertaken at room temperature and UV irradiation, using the decomposition of *diquat* as test reaction. This recognized toxic organic substance is normally used as herbicide to pest control.

The kinetics of photocatalytic degradation of organic compounds usually follows the Langmuir–Hinshelwood kinetics model [6], simplified to the apparent rate order equation:

$$\ln\left(\frac{C_0}{C}\right) = kKt = K_{app}t$$

where C is the concentration of the organic pollutant, t is the irradiation time, k the rate constant of the reaction and K is the adsorption coefficient of the organic pollutant. The apparent first order rate constant, K_{app}, is given by the slope of the graph of ln (C_0/C) versus t, C_0 corresponding to the initial concentration of the organic pollutant.

The results of the kinetics degradation of *diquat* under UV irradiation are presented in Fig. 7, and the determined K_{app} values

Table 4
Bandgap (E_g) and absorption edge values (λ_g) of M:TiO_2 powders.

Samples	E_g (eV)	λ_g (nm)
TiO_2 [26]	3.25	382
Fe:TiO_2	3.03	410
Sb:TiO_2	3.15	394
Nb:TiO_2	3.25	382
Co:TiO_2	2.96	419

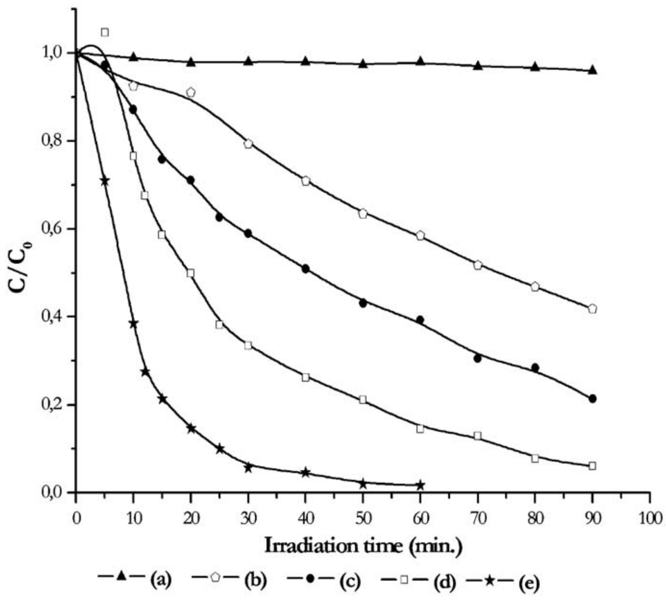

Fig. 7. Kinetics of *diquat* degradation under UV light irradiation for the photocatalysts powders: without catalyst (▲), in the presence of commercial P25 (⬠), undoped TiO_2 (●), Nb:TiO_2 (□) and Sb:TiO_2 (★).

Table 5
Apparent first order rate constants (K_{app}) and corresponding correlation coefficient (r) for *diquat* degradation (10^{-4} M), under UV irradiation.

Catalyst	K_{app} (min^{-1})	r
TiO_2	0.016	0.994
Sb:doped	0.090	0.992
Nb:doped	0.031	0.991
P25	0.010	0.995

are given in Table 5. The curves using Fe:TiO_2 and Co:TiO_2 as catalysts were not included in this figure, since, in these cases, no photocatalytic activity was observed. The results obtained for the commercial TiO_2 (P25) were included for a comparative purpose. For Fe:TiO_2 and Co:TiO_2, visible radiation was also tested, but the photocatalytic results were the same, i.e., no significant degradation was observed.

The preliminary results here obtained evidence an appreciable enhancement in the photocatalytic efficiency of the Sb:TiO_2 and Nb:TiO_2 nanopowders, which exhibit a high photocatalytic activity under UV irradiation.

It was previously stated that dopants with a closed-shell electronic configuration, such as Sb^V and Nb^V have little effect on photoreactivity [19]. Nevertheless such fact is questionable, since other literature reports demonstrated different behaviours. For example, Karakitsou et al. [38] showed that doping with cations of valency higher than that of Ti^{IV} enhanced the performance of the doped TiO_2 photocatalyst for water cleavage. Significantly improved photocatalytic performance for the methylene blue degradation was also obtained with Sb-doped TiO_2 prepared by a coprecipitation method [39].

The present Mössbauer results clearly show that in Sb:TiO_2 nanopowder, the antimony coexist in two oxidation states in the TiO_2 lattice, Sb^{III} and Sb^V. Considering that Nb^V is the most probable oxidation sate of this metal, this is certainly the most abundant ion present in the prepared compound. Additionally, oxidative synthesis conditions used should maintain Nb ions in their higher oxidation state, supporting this hypothesis. Since the ionic radius of Nb^{5+} (i.r $= 0.64$ Å) is very similar to Ti^{4+} (i.r $= 0.61$ Å), it is expected that niobium dopant act as donor atom when dissolved in the TiO_2 lattice, due to charge transfer to TiO_2 conduction band [40]. Therefore, the charge compensation due to substitution of Ti^{IV} by Nb^V, would be achieved either by creation of cation vacancies or stoichiometric reduction of Ti^{IV} to Ti^{III} per niobium incorporated [41]. In addition, the thermodynamic stability study performed with Nb:TiO_2 nanopowder reinforces our assumption, once the absence of oxygen vacancies seem to be a plausible explanation for the hindrance of anatase to rutile transformation. Thus, it seems clear that doping with Sb^V (d^{10}) and Nb^V (d^0) ions, with valence higher than Ti^{IV}, leads to a better performance of the photocatalysts in the present study. The highest photocatalytic activity observed for Sb:TiO_2 when compared with Nb:TiO_2 may be attributed to the presence of mixed valence ions in the case of antimony (Sb^{III} and Sb^V), and therefore to an electronic charge transfer higher for Sb:TiO_2 than for Nb:TiO_2 catalysts.

In the case of iron and cobalt doping, for which no photocatalytic activity was detected, and even if a decrease of the band gap was observed, the doped ions are Fe^{III} (d^5), Co^{III} (d^6) and Co^{IV} (d^5), as determined by ^{57}Fe Mössbauer spectroscopy and magnetization measurements, leading to a mean valence of the doped ions inferior to IV. For these samples, the substitution of Ti^{IV} ions by Co^{III} and Co^{IV} (Co:TiO_2) and Fe^{III} (Fe:TiO_2) will probably create oxygen vacancies in the TiO_2 lattice. These vacancies may behave as electron traps resulting in the decrease of electrons in the conduction band, thus reducing the photocatalytic efficiency.

Moreover, in the case of Fe:TiO_2 and Co:TiO_2, the red shift observed in the bandgap, can be assigned to the charge-transfer transition from the d orbital of Fe^{III} and Co^{III}/Co^{IV}, to the valence band of TiO_2 lattice, respectively. According to Jasra et al. [23] this fact is detrimental for the photocatalytic efficiencies, due to the reduction of the free charge carriers lifetime.

4. Conclusions

In the present work, doped titanium dioxide nanopowders (M:TiO_2; $M =$ Fe, Co, Nb, Sb) with anatase structure were successfully synthesized and characterized.

The thermodynamic stability of the samples allowed to conclude that the doping with antimony and niobium was undoubtedly achieved, as no impurity phases were detected by XRD after the calcinations up to 1100 °C. In the case of the iron and cobalt doping, the effective doping amount can be smaller than the nominal value (5%). This study also clearly showed that the anatase structure, observed for all doped samples, is highly stable. In the case of Nb:TiO_2 and Sb:TiO_2 phases, the anatase structure remains pure and stable up to 900 and 800 °C, respectively.

Mössbauer spectroscopy studies clearly indicated the presence of both Sb^{III} and Sb^V ions for the Sb:TiO_2 sample, whereas only Fe^{III} is present in the iron doped TiO_2 compound. In the case of the Co:TiO_2 sample, a mixed oxidation state for cobalt ions was deduced from the magnetization results.

Significant differences on the photocatalytic behaviour of the prepared M:TiO_2 samples were found, but it was not possible to extend its photoresponse to visible light. An appreciable enhancement in the photocatalytic efficiency of the Sb:TiO_2 and Nb:TiO_2 nanopowders was observed under UV irradiation, but no photocatalytic activity was detected for the Fe:TiO_2 and Co:TiO_2 samples.

These results demonstrate that the synthesis method used in the present work is auspicious to prepare highly active photocatalysts Nb:TiO_2 and especially Sb:TiO_2, which proved to be the best one. Besides, it can be concluded that both doped metal content and valence of the doping ions are crucial factors that strongly determine the photocatalytic activity of these compounds for *diquat* degradation.

Acknowledgements

Ana L. Castro thanks FCT for the PhD grants (SFRH/BD/19073/2004).

References

[1] M.A. Fox, M.T. Dulay, Chem. Rev. 93 (1993) 341–357.
[2] M.R. Hoffmann, S.T. Martin, W. Choi, D.W. Bahnemann, Chem. Rev. 95 (1995) 69–96.
[3] A. Mills, S.L. Hunte, J. Photochem. Photobiol. A: Chem. 108 (1997) 1–35.
[4] A.L. Linsebigler, G. Lu, J.T. Yates, Chem. Rev. 95 (1995) 735–758.
[5] M. Anpo, Pure Appl. Chem. 72 (2000) 1265–1270.
[6] I.K. Konstantinou, T.A. Albanis, Appl. Catal. B: Environ. 42 (2003) 319–335.
[7] J.-M. Herrmann, Catal. Today 53 (1999) 115–129.
[8] J.-M. Herrmann, Top. Catal. 34 (2005) 49–65.
[9] C. He, Y. Yu, X. Hu, A. Larbot, Appl. Surf. Sci. 200 (2002) 239–247.
[10] A.G. Agrios, P. Pichat, J. Appl. Electrochem. 35 (2005) 655–663.
[11] M. Kitano, M. Matsouka, M. Ueshima, M. Anpo, Appl. Catal. A: Gen. 325 (2007) 1–14.
[12] Y. Liu, X. Chen, J. Li, C. Burda, Chemosphere 61 (2005) 11–18.
[13] H.-H. Ou, S.-L. Lo, J. Mol. Catal. A: Chem. 275 (2007) 200–205.
[14] S. Liao, H. Donggen, D. Yu, Y. Su, G. Yuan, J. Photochem. Photobiol. A: Chem. 168 (2004) 7–13.
[15] J. Aguado, R. Grieken, M.-J. López-Muñoz, J. Marugán, Appl. Catal. A: Gen. 312 (2006) 202–212.

[16] L. Zou, Y. Luo, M. Hooper, E. Hu, Chem. Eng. Process. 45 (2006) 959–964.
[17] Y. Bessekhouad, D. Robert, J.-V. Weber, N. Chaoui, J. Photochem. Photobiol. A: Chem. 167 (2004) 49–57.
[18] M. Saif, M.S.A. Abdel-Mottaleb, Inorg. Chim. Acta 360 (2007) 2863–2874.
[19] W. Choi, A. Termin, M.R. Hoffmann, J. Phys. Chem. 98 (1994) 13669–13679.
[20] S.T. Martin, C.L. Morrison, M.R. Hoffmann, J. Phys. Chem. 98 (1994) 13695–13704.
[21] A. Fuerte, M.D. Hernández-Alonso, A.J. Maira, A. Martínez-Arias, M. Fernández-García, J.C. Conesa, J. Soria, Chem. Commun. (2001) 2718–2719.
[22] S. Karvinen, Solid State Sci. 5 (2003) 811–819.
[23] R.J. Tayade, R.G. Kulkarni, R.V. Jasra, Ind. Eng. Chem. Res. 45 (2006) 5231–5238.
[24] M. Bellardita, M. Addamo, A.D. Paola, L. Palmisano, Chem. Phys. 339 (2007) 94–103.
[25] A.L. Castro, M.R. Nunes, A.P. Carvalho, F.M. Costa, M.H. Florêncio, Solid State Sci. 10 (2008) 602–606.
[26] J. Zhu, F. Chen, J. Zhang, H. Chen, M. Anpo, J. Photochem. Photobiol. A: Chem. 180 (2006) 196–204.
[27] L. Diamandescu, F. Vasiliu, D. Tarabasanu-Mihaila, M. Feder, A.M. Vlaicu, C.M. Teodorescu, D. Macovei, I. Enculescu, V. Parvulescu, E. Vasile, Mater. Chem. Phys. 112 (2008) 146–153.
[28] Z. Ambrus, N. Balázs, T. Alapi, G. Wittmann, P. Sipos, A. Dombi, K. Mogyorósi, Appl. Catal. B: Environ. 81 (2008) 27–37.
[29] M.R. Nunes, O.C. Monteiro, A.L. Castro, D.A. Vasconcelos, A.J. Silvestre, Eur. J. Inorg. Chem. (2008) 961–965.
[30] T. Roisnel, J. Rodriguez-Carvajal, FullProf Suite, April 2005.
[31] K. Rubenbauer, T. Birchall, Hyperfine Interact 7 (1979) 125–133.
[32] E.P. Day, Methods Enzymol. 227 (1993) 437–463.
[33] K.M. Reddy, S.V. Manorama, A.R. Reddy, Mater. Chem. Phys. 78 (2002) 239–245.
[34] M.H. Florêncio, E. Pires, A.L. Castro, M.R. Nunes, C. Borges, F.M. Costa, Chemosphere 55 (2004) 345.
[35] M. Nag, P. Basak, S.V. Manorama, Mater. Res. Bull. 42 (2007) 1691–1704.
[36] M.A. Barakat, G. Hayes, S.I. Shah, J. Nanosci. Nanotechnol. 5 (2005) 759–765.
[37] D.J. Stewart, O. Knop, C. Ayasse, F.W.D. Woodhams, Can. J. Chem. 50 (1972) 690–700.
[38] K.E. Karakitsou, X.E. Verykios, J. Phys. Chem. 97 (1993) 1184–1189.
[39] J. Moon, H. Takagi, Y. Fujishiro, M. Awano, J. Mater. Sci. 36 (2001) 949–955.
[40] A. Mattsson, M. Leideborg, K. Larsson, G. Westin, L. Sterlund, J. Phys. Chem. B 110 (2006) 1210–1220.
[41] A.M. Ruiz, G. Dezanneau, J. Arbio, A. Cornet, J.R. Morante, Chem. Mater. 16 (2004) 862–871.